

Article

# Pore Structure Characteristics and Reservoir Classification of Tight Sandstones within the Upper Permian Longtan Formation in the Laoshan Uplift, South Yellow Sea Basin: Implications for Hydrocarbon Exploration

Haoran Zhang <sup>1</sup>, Yong Yuan <sup>2,3,4,\*</sup>, Jianwen Chen <sup>2,3</sup>, Jie Liang <sup>2,3,4</sup> and Hualin Zhao <sup>2</sup>

<sup>1</sup> College of Oceanography, Hohai University, Nanjing 210024, China; hhuzhanghr@163.com

<sup>2</sup> Qingdao Institute of Marine Geology, China Geological Survey, Qingdao 266237, China; jwchen2012@126.com (J.C.); cgsljie@mail.cgs.gov.cn (J.L.); zhaohualin2020@163.com (H.Z.)

<sup>3</sup> Laboratory for Marine Mineral Resources, Qingdao Marine Science and Technology Center, Qingdao 266237, China

<sup>4</sup> School of Marine Geosciences, Ocean University of China, Qingdao 266100, China

\* Correspondence: yuany010@126.com

**Abstract:** The Upper Permian Longtan Formation in the Laoshan Uplift of the South Yellow Sea Basin hosts thick and distinctive tight sandstones. However, a comprehensive understanding of its pore structure and reservoir classification remains lacking. This study investigates the fully cored well, CSDP-2, utilizing thin section analysis, scanning electron microscopy, energy spectrum analysis, X-ray diffraction, high-pressure mercury intrusion, and nuclear magnetic resonance to characterize its petrophysical properties, pore space, and movable fluid characteristics. Additionally, fractal principles are further employed to examine reservoir heterogeneity and conduct a quantitative assessment, considering the complexity of tight sandstone pore structures. The findings reveal that the sandstones predominantly comprise feldspathic litharenites, with an average porosity of 1.567% and permeability of 0.099 mD, primarily containing intragranular pores. Two distinct sets of pores with significantly different sizes ( $r < 2 \mu\text{m}$ ;  $r > 6 \mu\text{m}$ ) were identified, displaying relatively high fractal dimensions and discrete distribution. Movable fluids primarily occupy pores with radii  $> 0.019 \mu\text{m}$ , reflecting pronounced overall heterogeneity. The reservoir was classified into three categories utilizing permeability, median radius, and movable fluid saturation as key evaluation parameters, with Class I representing a relatively high-quality reservoir. These findings advance our understanding of the pore development mechanism of tight sandstone reservoirs and provide geological evidence for further hydrocarbon exploration in this study area.

**Keywords:** tight sandstone; pore structure; fractal; reservoir evaluation; Laoshan Uplift; South Yellow Sea Basin



**Citation:** Zhang, H.; Yuan, Y.; Chen, J.; Liang, J.; Zhao, H. Pore Structure Characteristics and Reservoir Classification of Tight Sandstones within the Upper Permian Longtan Formation in the Laoshan Uplift, South Yellow Sea Basin: Implications for Hydrocarbon Exploration. *J. Mar. Sci. Eng.* **2024**, *12*, 732. <https://doi.org/10.3390/jmse12050732>

Academic Editor: Hailong Lu

Received: 23 March 2024

Revised: 25 April 2024

Accepted: 26 April 2024

Published: 28 April 2024



**Copyright:** © 2024 by the authors. Licensee MDPI, Basel, Switzerland. This article is an open access article distributed under the terms and conditions of the Creative Commons Attribution (CC BY) license (<https://creativecommons.org/licenses/by/4.0/>).

## 1. Introduction

As conventional oil and gas reserves dwindle, attention has shifted towards unconventional resources, notably tight sandstone oil and gas reservoirs with matrix permeability of less than 0.1 mD and porosity of less than 10%, which have seen significant development globally [1–5]. In China, exploration efforts have been concentrated in basins such as the Sichuan, Ordos, Tarim, Junggar, and Songliao. In 2021, tight sandstone gas and oil production in these locations totaled approximately  $526 \times 10^8 \text{ m}^3$  and  $300 \times 10^4 \text{ t}$ , respectively [6].

Permian tight sandstone, particularly in the northern Ordos Basin, is crucial for unconventional oil and gas exploration. Notably, the Sulige Gas Field, the largest onshore integrated tight sandstone gas field in China, has seen annual gas production surpassing  $230 \times 10^8 \text{ m}^3$  since 2014, reaching more than  $260 \times 10^8 \text{ m}^3$  in 2020 [7–9]. The Linxing Gas

Field, located in the Permian He 2 Member tight sandstone reservoir at the eastern margin of the Ordos Basin, has emerged as one of the largest gas fields in this basin [10]. In the Bohai Bay Basin, significant oil and gas flows have been discovered in the Permian Upper Shihezi Member tight sandstone, notably at the well sites such as Guangu 1601, Yinggu 1, and Yinggu 2 in the southern Dagang area [11]. Furthermore, Well Hua 3 in the Huangqiao area of the Lower Yangtze region has achieved a daily oil production of 1.5 tons from the Longtan tight sandstones, nearing industrial capacity [12]. Variations in pore-volume abundance, pore size, and pore-network connectivity in tight sandstones significantly influence hydrocarbon storage capacity and deliverability [5,13,14]. A comprehensive understanding of the heterogeneous pore structure is crucial for the successful exploration and development of these tight sandstone reservoirs [2,3,5,15,16].

The South Yellow Sea Basin, adjacent to the onshore Lower Yangtze region, has similar geological structures to that region. With a relatively complete development of Paleozoic-Mesozoic marine strata, it exhibits multi-source and multi-stage accumulation characteristics that could signify the formation of large oil and gas fields [17,18]. However, no significant hydrocarbon exploration breakthroughs have yet occurred in this basin.

In recent years, advances in seismic detection technology and drilling—notably the full-core drilling well CSDP-2, carried out in the Laoshan Uplift of the South Yellow Sea Basin—have confirmed thick layers of tight sandstones in the Upper Permian Longtan Formation, with multiple oil and gas indications [18,19]. While previous studies of the Longtan Formation in the Laoshan Uplift, situated in the central part of the basin with promising hydrocarbon exploration potential, have provided valuable insights into its seismic stratigraphy, tectonic evolution [17,20], sedimentary environments [21,22], source rock characteristics [23,24], and reservoir features [25], research on the pore structure of this formation remains insufficient, and a systematic understanding of reservoir quality has not been established.

This paper presents an in-depth study conducted on the petrophysical properties, pore structure characteristics, and movable fluid features of the Longtan tight sandstones collected from Well CSDP-2. Additionally, fractal theory was employed to discuss Longtan tight sandstone reservoir heterogeneity, and multiple parameters were integrated to classify and evaluate this reservoir, providing further theoretical support for the investigation and exploration of hydrocarbons in the South Yellow Sea Basin.

## 2. Geological Setting

Situated in the eastern waters of China, the South Yellow Sea spans an area of approximately  $3 \times 10^5$  km<sup>2</sup> [26–28]. Tectonically, it extends from the Yangtze Platform into the sea area and represents the primary section of the Lower Yangtze region [28]. The South Yellow Sea Basin originated on the Archean-Proterozoic metamorphic basement, over which Paleozoic-Mesozoic marine and Mesozoic-Cenozoic continental sedimentary basins were superimposed [17,28]. Geologically, the basin comprises three secondary tectonic units: the Yantai Depression, Laoshan Uplift, and Qingdao Depression, arranged respectively from north to south (Figure 1).

To date, only 30 wells have been drilled, primarily concentrated in the Yantai and Qingdao Depressions [19]. Notably, Well CSDP-2, drilled in 2016, marked the first drilling endeavor in the Laoshan Uplift. This well achieved a depth of 2843.18 m, with an impressive average core recovery rate of 97.7%. It successfully penetrated through the Triassic, Permian, Carboniferous, Devonian, and Silurian strata beneath the Neogene strata [18]. Specifically, the Upper Permian Longtan Formation, with a thickness of approximately 453.4 m, primarily comprises littoral swamp and deltaic deposits, with the predominant lithological constituents including black mudstone, coal seams, and gray silt-fine sandstone [22,23,25].

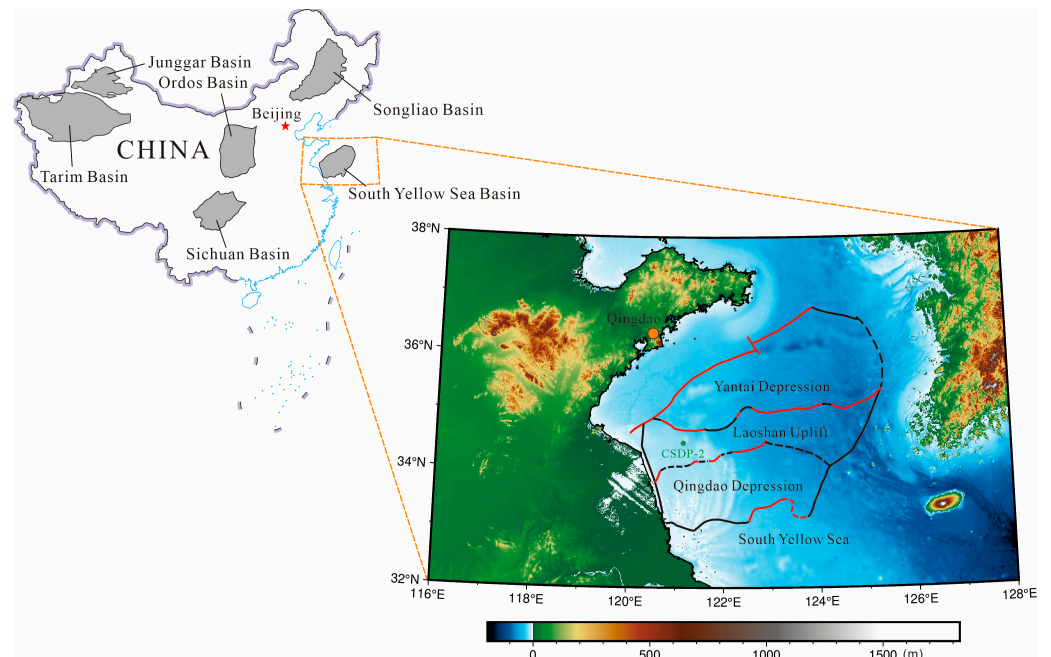


**Figure 1.** Regional location and tectonic zoning of the South Yellow Sea Basin [17,28]. Digital elevation data source: <https://www.generic-mapping-tools.org> (accessed on 30 October 2023).

### 3. Materials and Methods

#### 3.1. Samples and Experimental Methods

Tight sandstone samples were selected from 1020 to 1175 m depths of the Upper Permian Longtan Formation from Well CSDP-2. Subsequent analysis focused on petrological characteristics, physical properties, pore structure, and movable fluid properties.

The identification of minerals such as quartz, feldspar, carbonate, and clay minerals in the samples was conducted using a LEICA DM2500 P polarizing microscope (Leica Microsystems, Wetzlar, Germany). Prior to observation, thin sections underwent cleaning, polishing, and staining with a mixture of alizarin red-S and potassium ferrocyanide solutions to enhance the identification of carbonate minerals. Additionally, epoxy resin-stained thin sections were prepared for examining the pore structure. Mineral composition was determined using a Dmax-2500 X-ray diffractometer (Rigaku Corporation, Tokyo, Japan) under specific conditions: 40 kV accelerating voltage, 40 mA current,  $0.02^\circ$  scanning step, 2 s time step, and  $2\theta$  range from  $0^\circ$  to  $50^\circ$ . Scanning electron microscopy and energy spectrum analysis were carried out using a MIRA 3 thermal field emission scanning electron microscope (TESCAN, Brno, Czech Republic) equipped with an Oxford X-Max SDD energy dispersive spectrometer (Oxford Instruments plc, Abingdon, UK). The operating parameters included an acceleration voltage of 10–20 kV and a working distance ranging from approximately 5 to 15 mm.

Reservoir petrophysical property testing and analysis were performed on core plugs measuring 2.5 cm in diameter. This was accomplished using an AP-608 automated permeameter-porosimeter (pressure sensor accuracy  $\pm 0.1\%$ ; Coretest Systems Inc., Morgan Hill, CA, USA) to measure porosity and permeability at  $19^\circ\text{C}$ , 30% humidity, and an atmospheric pressure of 1031 hPa. The AP-608 instrument is cost-effective and applied Boyle's law to measure the porosity and Klinkenberg effect to measure the permeability. For nuclear magnetic resonance (NMR) analysis, the above core plugs were cleaned oil and saturated in a NaCl saline solution under vacuum for 24 h. NIUMAG MicroMR series NMR core analyzers (Niumag Corporation, Shanghai, China) were used, employing a Carr–Purcell–Meiboom–Gill sequence with specific parameters: a main radiofrequency signal frequency of 12 MHz, an RF signal frequency offset of 100,673.89 Hz, a sampling bandwidth of 250 kHz, a repetition sampling interval of 4000 ms, an echo time of 0.1 ms,

8000 echoes, a preamplifier gain of 3, and 32 scans. High-pressure mercury intrusion (HPMI) experiments were conducted using a MicroActive AutoPore V-9600 fully automatic mercury intrusion porosimeter (Micromeritics Instrument Corporation, Norcross, GA, USA). This experiment, recognized for its invasive and destructive nature, was carried out as the concluding experimental procedure. Samples, which were cut into 1 cm<sup>3</sup> cubes and pre-treated by drying in an oven at 70 °C for over 48 h, were subjected to pressures ranging from 0 to 420.9 MPa, with a contact angle of 130°.

### 3.2. Fractal Theory and Computational Methods

Fractal theory offers a methodology to explore the internal structure of irregular bodies through self-similarity [29]. Objects exhibiting fractal characteristics are described by the fractal dimension *D*, which can be used to quantify the complexity and irregularity of reservoir pore structures, with values typically ranging between two and three [30]. A *D* value nearing two indicates greater reservoir homogeneity and simpler pore structures, while a *D* value closer to three suggests heightened reservoir heterogeneity and more complex pore structures [31,32].

According to fractal theory, the cumulative volume percentage *S*(<*r*) of pores with diameters smaller than *r* in the reservoir can be expressed as follows [29]:

$$S(< r) = \frac{r^{3-D} - r_{\min}^{3-D}}{r_{\max}^{3-D} - r_{\min}^{3-D}} \tag{1}$$

where *r* denotes the pore radius (μm), *r*<sub>min</sub> stands for the minimum pore radius, *r*<sub>max</sub> represents the maximum pore radius, *S*(*r*) is the density distribution function of the pore radius, and *D* is the fractal dimension.

In HPMI experiments, Equation (1) can be reformulated in terms of mercury saturation as follows:

$$S(< r) = 1 - S_{\text{Hg}} = \frac{r^{3-D_P} - r_{\min}^{3-D_P}}{r_{\max}^{3-D_P} - r_{\min}^{3-D_P}} \tag{2}$$

where *S*<sub>Hg</sub> represents the cumulative mercury saturation (%) when the pore radius is *r*, and *D*<sub>P</sub> is the fractal dimension of HPMI. Due to *r*<sub>max</sub> ≫ *r*<sub>min</sub>, Equation (2) simplifies to

$$S(< r) = 1 - S_{\text{Hg}} = \frac{r^{3-D_P}}{r_{\max}^{3-D_P}} \tag{3}$$

Taking the logarithm of Equation (3), the formula for computing the fractal dimension *D*<sub>P</sub> based on pore size in HPMI experiments is derived as follows:

$$\log(1 - S_{\text{Hg}}) = (3 - D_P)\log r - (3 - D_P)\log r_{\max} \tag{4}$$

Equation (4) reveals a linear relationship between log(1 - *S*<sub>Hg</sub>) and log*r*. The fractal dimension *D*<sub>P</sub> can therefore be determined using double logarithmic coordinates.

In contrast to HPMI experiments, which directly correlate pore size and volume, NMR testing typically utilizes the transverse relaxation time *T*<sub>2</sub> to reflect surface relaxation determined by the specific surface area and relaxation rate [33]. The relationship between *T*<sub>2</sub> and *r* is expressed by the following equation:

$$\frac{1}{T_2} = \rho \left( \frac{S}{V} \right) = F_s \frac{\rho}{r} \tag{5}$$

where *ρ* denotes the surface relaxation rate (considered constant), *T*<sub>2</sub> represents the transverse relaxation time (m/ms), *S*/*V* is the ratio of pore space surface area to volume. *F*<sub>s</sub> is a constant geometric shape factor, where *F*<sub>s</sub> equals 1, 2, or 3 for planar, cylindrical, and spherical models, respectively [33]. For this study, cylindrical pores are assumed, and the constant value (*F*<sub>s</sub>) is set to 2.

According to Equation (5),  $T_2$  obtained from NMR experiments is directly proportional to the ratio of specific surface area and pore size, with  $r_{max}$  corresponding to  $T_{2max}$  and  $r_{min}$  corresponding to  $T_{2min}$ . Combined with Equation (1), the fractal dimension  $D_N$  obtained based on NMR testing  $T_2$  values can be expressed as follows:

$$S(< r) = \frac{T_2^{3-D_N} - T_{2min}^{3-D_N}}{T_{2max}^{3-D_N} - T_{2min}^{3-D_N}} \tag{6}$$

Since  $T_{2max} \gg T_{2min}$ , Equation (6) simplifies to

$$S(< r) = \frac{T_2^{3-D_N}}{T_{2max}^{3-D_N}} \tag{7}$$

Taking the logarithm of Equation (7), we obtain

$$\log(S(< r)) = (3 - D_N)\log(T_2) - (3 - D_N)\log T_{2max} \tag{8}$$

There exists a linear relationship between  $\log(S(<r))$  and  $\log T_2$ . Under the condition of satisfying the fractal theory, the fractal dimension  $D_N$  can be determined using double logarithmic coordinates in NMR experiments.

#### 4. Results

##### 4.1. Petrophysical Properties, Lithological Characteristics, and Pore Types

The porosity of Longtan Formation samples from Well CSDP-2 ranges from 1.192% to 2.323%, with the permeability varying between 0.000259 and 0.9185 mD, indicating typical tight sandstones (Table 1).

**Table 1.** Summary of petrophysical properties, high-pressure mercury injection, and nuclear magnetic resonance parameters of the Longtan tight sandstones of Well CSDP-2, South Yellow Sea Basin.

Sample No.	Well Depth/m	Petrophysical Characteristics		High-Pressure Mercury Injection Test				Nuclear Magnetic Resonance Test		
		Porosity/%	Permeability/mD	Maximum Mercury Saturation/%	Threshold Pressure/MPa	Average Pore Radius/ $\mu$ m	Median Radius/ $\mu$ m	$T_{2Cut-off}$ /ms	Movable Fluid Saturation/%	Bound Fluid Saturation/%
G-21	1020.00	1.958	0.01014	96.52	0.002691	1.4112	222.57	0.51	6.54	93.46
G-22	1030.00	1.210	0.012	89.78	0.006762	0.02167	185.58	1.87	5.65	94.35
C-3	1110.8	2.054	0.0154	98.16	0.069138	0.02915	183.34	1.15	18.48	81.52
C-4	1114.7	1.216	0.000259	95.03	0.047196	0.1108	202.47	1.06	12.83	87.17
C-5	1121.25	1.314	0.1036	99.74	0.016491	0.01413	82.68	0.98	7.52	92.48
C-6	1125.00	1.292	0.0246	93.20	0.005037	0.08554	121.95	1.25	11.37	88.63
C-8	1135.00	1.395	0.000634	73.60	0.003864	0.04688	132.79	0.71	9.50	90.50
C-14	1157.00	1.192	0.00275	88.38	0.165462	0.9472	235.29	4.94	5.84	94.16
C-16	1161.00	2.323	0.9185	85.28	0.050094	0.07395	331.76	8.7	34.83	65.17
C-19	1167.00	1.933	0.00206	98.24	0.053682	0.29405	265.56	0.47	7.00	93.00
C-22	1175.00	1.439	0.00374	97.60	0.079212	0.04882	206.06	0.9	23.72	76.28

The Longtan Formation consists mainly of tight sandstones with linear contacts, with some samples exhibiting concave-convex contacts. Comprising mainly fine sandstones and siltstones, the predominant grain size ranges from 0.09 to 0.25 mm, featuring subangular to subrounded grain shapes. X-ray diffraction analysis indicates that the detrital components of the Longtan tight sandstone of Well CSDP-2 primarily comprise quartz and feldspar (Table 2). The quartz content predominantly falls within the range of 59.8% to 78.0%, with an average of 67.8%. Following quartz, the feldspar content ranges from 4.1% to 26.3%, with an average content of 16.1%. The prevailing sandstone type is feldspathic litharenite. Observations from thin sections and scanning electron microscopes reveal that the studied tight sandstones primarily develop intragranular dissolution pores (Figure 2c,d), alongside residual minor amounts of intergranular pores and developed fractures (Figure 2a,b,e).

**Table 2.** Relative content of sandstone minerals in the Longtan tight sandstones in Well CSDP-2.

Sample No.	Quartz (%)	Feldspar (%)	Calcite (%)	Pyrite (%)	Clay Minerals (%)
C-5	64.2	22.2			13.6
C-6	67.1	22.3	0.8		9.8
C-8	75.9	13.1			11.1
C-14	59.8	14.0			26.3
C-16	78.0	14.2	2.2	1.4	4.1
G-21	67.6	13.2			19.2
G-22	65.8	18.0			16.2

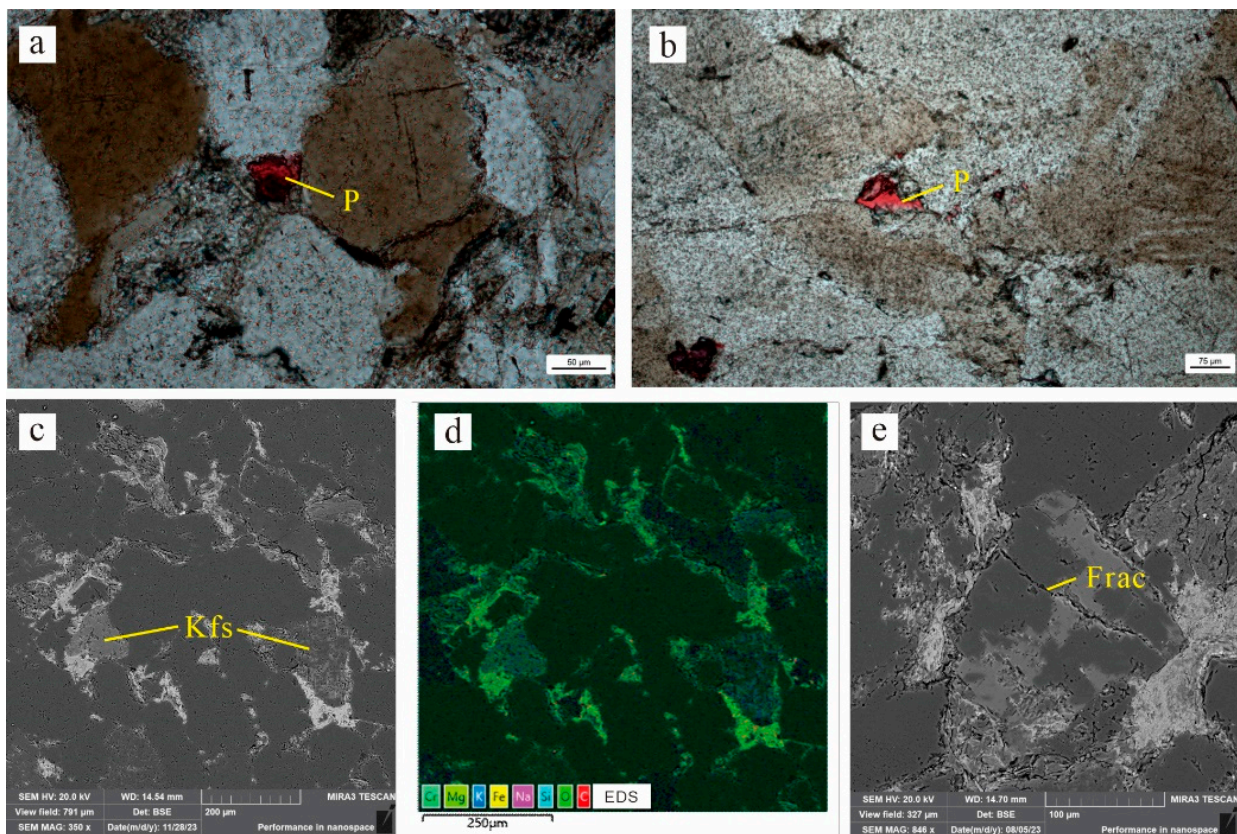


**Figure 2.** Microscopic characteristics of pore space in the Longtan tight sandstones, Well CSDP-2. (a) Development of residual intergranular pores, plane-polarized light, C-8, 1135.00 m; (b) development of residual intergranular pores, plane-polarized light, C-16, 1161.00 m; (c) SEM image showing development of intragranular dissolution pores in potassium feldspar grains, C-8, 1135.00 m; (d) corresponding energy spectrum scan result to (c). EDS—energy dispersive spectroscopy. Color-coded EDS element maps are overlaid on SEM images; (e) SEM image showing development of micro-fractures within grains, C-8, 1135.00 m. P—pore; Kfs—potassium feldspar; frac—micro-fractures/cracks; SEM—scanning electron microscope.

#### 4.2. Pore structure Characteristics

##### 4.2.1. High-Pressure Mercury Injection Characteristics

HPMI analysis enables both qualitative and quantitative analysis of the inherent pore structure characteristics within the reservoir [34–36]. This is achieved by integrating capillary pressure curves with pore structure parameters. In the Longtan Formation of Well CSDP-2, the mercury saturation of tight sandstones ranges from 73.60% to 99.74%, with threshold pressures spanning 0.003 to 0.079 MPa. Various forms of capillary pressure curves are evident in the tight sandstone reservoirs of the study area (Figure 3a). Notably,

sample C-16 demonstrates the smoothest overall capillary pressure curve and exhibits superior petrophysical properties. Conversely, samples C-4 and C-8 display shorter smooth segments in their capillary pressure curves and are characterized by multiple broken line segments and frequent steep increases, indicating poorer petrophysical properties.

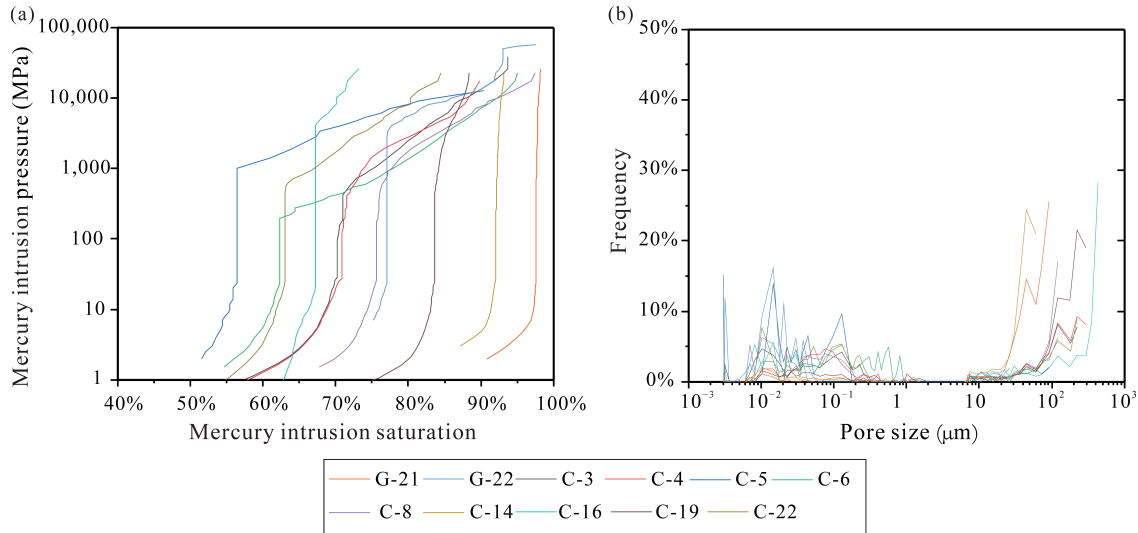


**Figure 3.** High-pressure mercury injection curves of the Longtan tight sandstones of Well CSDP-2. (a) Capillary pressure curves with the saturation profiles differing dramatically due to differences in pore size distribution; (b) pore size distribution curves indicating concentration primarily in the <2 μm and >6 μm intervals, with notable variations in frequency.

Analysis of HPMI pore size distribution curves reveals that the pore sizes are primarily concentrated in the <2 μm and >6 μm intervals (Figure 3b). The median pore radii of the samples in the study area vary from 82.68 to 331.76 μm, demonstrating significant discrepancies. These variations reflect the intricate structure and pronounced heterogeneity of the tight sandstones in the study area.

#### 4.2.2. Nuclear Magnetic Resonance Characteristics

The NMR  $T_2$  spectrum serves to depict the presence of water within core pores, and whether it is movable or bound (Figure 4a). The  $T_2$  cutoff value, denoted where the incremental curve of bound water reaches its apex and intersects with that of saturated water, delineates the boundary (as illustrated in Figure 4b). If  $T_2$  of the pore fluid exceeds the  $T_{2\text{cutoff}}$ , the fluid is classified as movable; otherwise, it is considered bound. The proportion of movable fluid in the total fluid is termed movable fluid saturation, while the percentage of bound fluid in total fluid is referred to as bound fluid saturation. Movable fluid saturation can serve as an indicator of reservoir fluid mobility, with lower levels indicating weaker corresponding reservoir storage and permeability [37–39]. In the study area, the distribution of movable fluid saturation among the Longtan sandstone samples ranges from 5.65% to 34.83%, with an average of 13.03%.

The  $T_2$  spectrum acquired through NMR can elucidate the pore size and distribution characteristics of rock samples, with longer  $T_2$  values corresponding to larger pore sizes [33,40]. A linear relationship between  $T_2$  spectrum and pore size exists, described as follows [41,42]:

$$r = CT_2 \tag{9}$$

Following the determination of the conversion coefficient  $C$  between  $T_2$  and the pore size (herein,  $C = 0.009 \mu\text{m}/\text{ms}$ ), the mutual conversion between NMR  $T_2$  spectrum and the pore radius can be conducted, enabling the calculation of the pore size distribution of the tight sandstone samples (Figure 5). Here, bound fluid predominantly occupies pores with

a radius of  $<0.019 \mu\text{m}$ , while movable fluid is primarily located in pores with a radius of  $>0.019 \mu\text{m}$ .

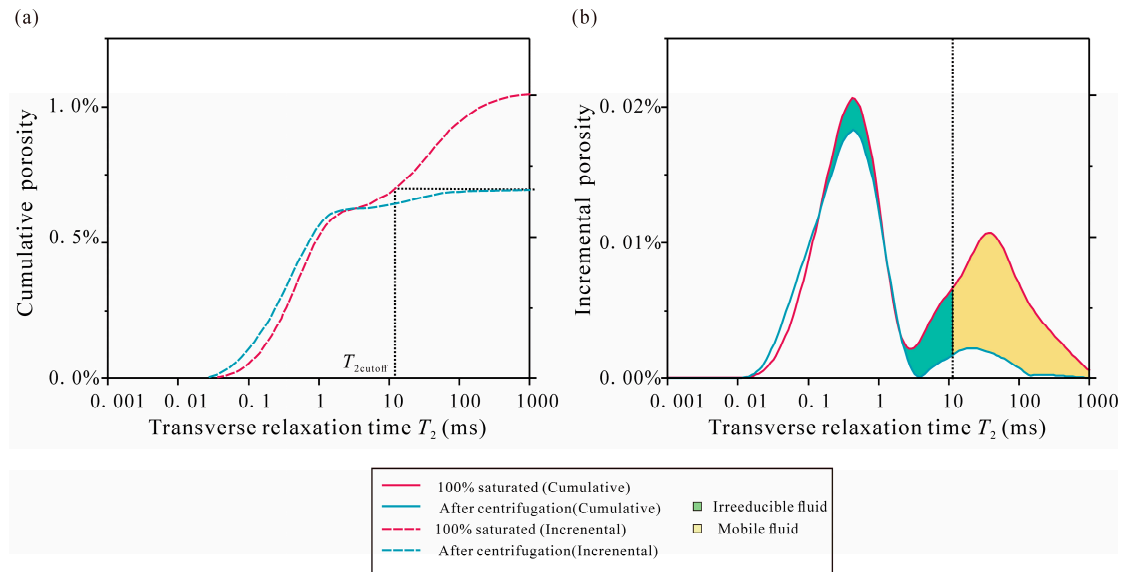


**Figure 4.** Distribution characteristics of nuclear magnetic resonance  $T_2$  spectra in Longtan tight sandstones in Well CSDP-2. (a) Schematic diagram of  $T_{2\text{cutoff}}$  value; (b) Schematic diagram of movable and bound fluid, C-16, 1161.00 m.

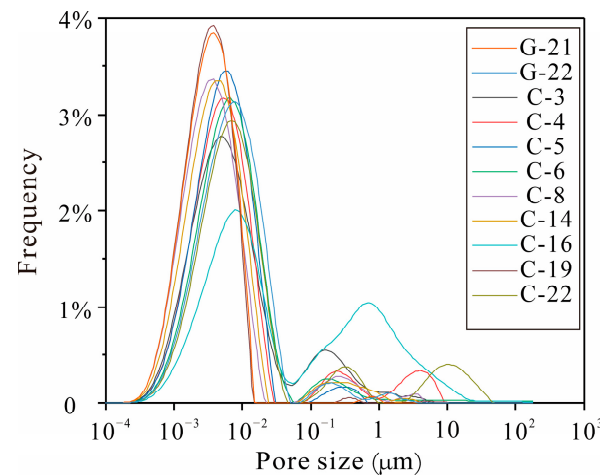


**Figure 5.** Pore size distribution of the Longtan tight sandstones of Well CSDP-2 obtained from nuclear magnetic resonance (NMR).

### 4.3. Fractal Characteristics

#### 4.3.1. Fractal Analysis of High-Pressure Mercury Injection in Tight Sandstone

The HPMI fractal curves of tight sandstone samples from Well CSDP-2 display segmented features. For representative samples (C-3, 1110.80 m; C-4, 1114.70 m), these fractal curves correspond to their respective pore size distributions. The relationship between  $\log(1 - S_{\text{Hg}})$  and  $\log r$  reveals two distinct inflection points (Figure 6). Based on this relationship, the pore space of the samples can be categorized into “large” and “small” pores.  $D_{P-1}$  represents the fractal dimension of small pores, associated with a pore radius of approximately  $<2 \mu\text{m}$ ; these fractal dimensions range from 2.22 to 2.96, with a mean of 2.68.  $D_{P-2}$  represents the fractal dimension of large pores, corresponding to a pore radius of approximately  $>6 \mu\text{m}$ ; these fractal dimensions range from 2.29 to 2.90, with a mean of 2.78 (Figure 6a; Table 3). The overall fractal dimension of the Longtan tight sandstones is

relatively high, suggesting considerable heterogeneity of the samples across various pore size intervals. The pore distribution exhibits discrete patterns.

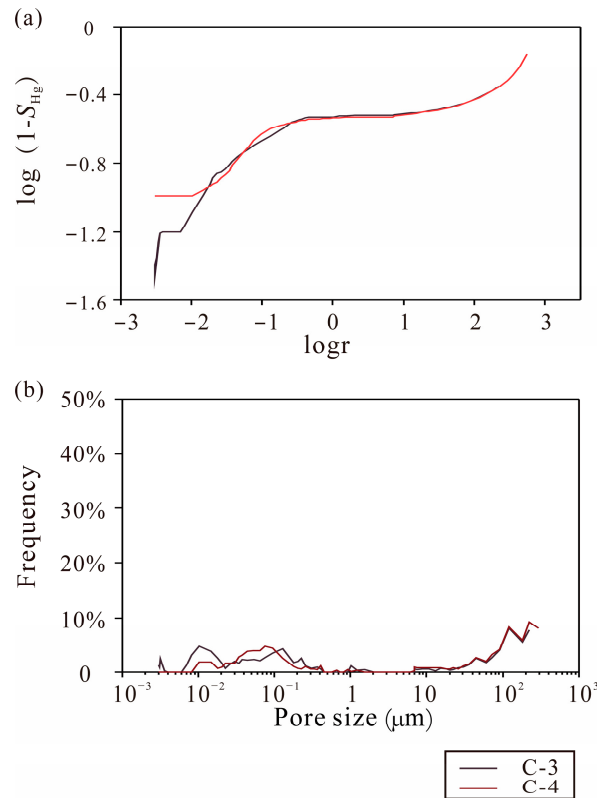


**Figure 6.** Fractal characteristic curves of high-pressure mercury injection in the Longtan tight sandstone samples, Well CSDP-2. (a) Different pore space fractal characteristics; (b) pore size distribution curve, C-3, 1110.80 m; C-4, 1114.70 m.

**Table 3.** Fractal dimensions of tight sandstone in the Longtan Formation of Well CSDP-2.

Sample No.	High-Pressure Mercury Injection				Nuclear Magnetic Resonance			
	Small Pores		Large Pores		$T_2 < T_{2\text{cutoff}}$		$T_2 > T_{2\text{cutoff}}$	
	$D_{P-1}$	$R^2$	$D_{P-2}$	$R^2$	$D_{N-1}$	$R^2$	$D_{N-2}$	$R^2$
G-21	2.94	0.87	2.29	0.94	-0.53	0.80	2.97	0.99
G-22	2.62	0.83	2.88	0.89	0.36	0.78	2.99	0.96
C-3	2.55	0.96	2.90	0.90	0.18	0.77	2.97	0.92
C-4	2.61	0.98	2.85	0.86	0.05	0.79	2.98	0.96
C-5	2.47	0.86	2.90	0.83	0	0.80	2.99	0.81
C-6	2.50	0.98	2.89	0.88	0.11	0.79	2.98	0.95
C-8	2.22	0.75	2.76	0.82	-0.26	0.78	2.98	0.94
C-14	2.96	0.94	2.52	0.92	1.01	0.69	2.99	0.86
C-16	2.95	0.85	2.90	0.98	1.01	0.70	2.94	0.83
C-19	2.90	0.96	2.77	0.78	-0.61	0.81	2.99	0.84
C-22	2.75	0.98	2.90	0.80	-0.13	0.81	2.98	0.94

#### 4.3.2. Fractal Analysis of Nuclear Magnetic Resonance in Tight Sandstone

The  $T_{2\text{cutoff}}$  value of tight sandstones in the study area functions as a critical point, delineating the scatter plot relationship curve of  $\log S_v$  and  $\log T_2$  for each sample into segments of  $T_2 < T_{2\text{cutoff}}$  and  $T_2 > T_{2\text{cutoff}}$  (Figure 7). These segments correspond to the fractal dimensions  $D_{N-1}$  and  $D_{N-2}$  of bound fluid and movable fluid, respectively. The fractal dimensions obtained from NMR for each sample were presented previously in Table 3. The fractal dimension  $D_{N-1}$  of bound fluid ranges from -0.53 to 1.01, with a

mean of 0.115, indicating that the pore space in the  $T_2 < T_{2\text{cutoff}}$  segment lacks fractal characteristics. Conversely, the fractal dimension  $D_{N-2}$  of movable fluid ranges from 2.94 to 2.99, with a mean of 2.977 and an average coefficient of determination  $R^2$  of 0.91, indicating that the pore space occupied by movable fluid demonstrates fractal characteristics, along with significant heterogeneity and complexity.

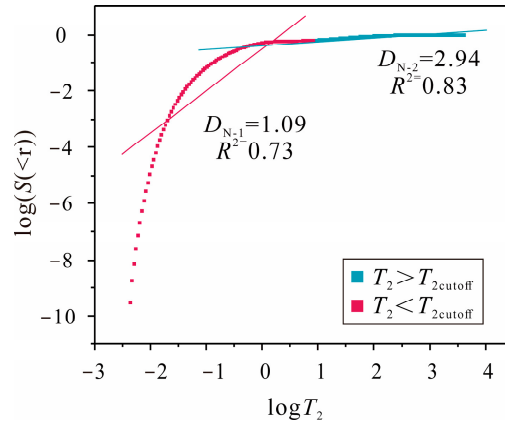


**Figure 7.** Fractal characteristic curves of nuclear magnetic resonance in the Longtan tight sandstone samples, Well CSDP-2, C-16, 1161.00 m. The scatter plot relationship curve exhibits two segments based on the  $T_{2\text{cutoff}}$  value.

## 5. Discussion

### 5.1. Variances in Full-Scale Pore Size Distribution Identified through Multiple Testing Methods

Numerous prior studies have indicated the intricate nature of the pore structure in tight sandstone, demonstrating significant heterogeneity; however, accurately characterizing its pore structure using a single testing method poses a challenge [43,44]. While each testing method can capture pore size information in tight sandstone, they all come with inherent limitations. Therefore, integrating multi-scale detection methods is crucial for its comprehensive characterization. Mercury, being a non-wetting phase, presents challenges in measuring pores smaller than 1.8 nm using HPMI analysis [45]. In NMR experiments, when calculating surface relaxation (the primary relaxation mechanism), the influence of diffusion relaxation is often not accounted for [46]. However, overlooking the diffusion relaxation mechanism in larger pores can introduce errors in pore size characterization [47].

Plotting the pore size distributions obtained from HPMI and NMR on the same coordinate system facilitates a more comprehensive characterization of the full-scale pore size distribution in the Longtan tight sandstones of Well CSDP-2 (Figure 8). Within the 0.001–1  $\mu\text{m}$  pore size range, the ranges of the pore size distribution curves for each sample generally coincide, with some consistency in peak position. However, due to the incremental pressurization in HPMI, the number of pressure points measured is fewer compared to the  $T_2$  spectrum test points, resulting in a piecewise linear shape instead of a smooth curve overall. Consequently, at the same pore size, the frequency of pore size distribution measured by HPMI is higher at the peak. For better pore size characterization of the studied Longtan tight sandstones,  $T_2$  spectrum test data are utilized for pore sizes  $< 1 \times 10^{-3} \mu\text{m}$ , while data obtained from HPMI are preferred for pore sizes  $> 6 \mu\text{m}$ .

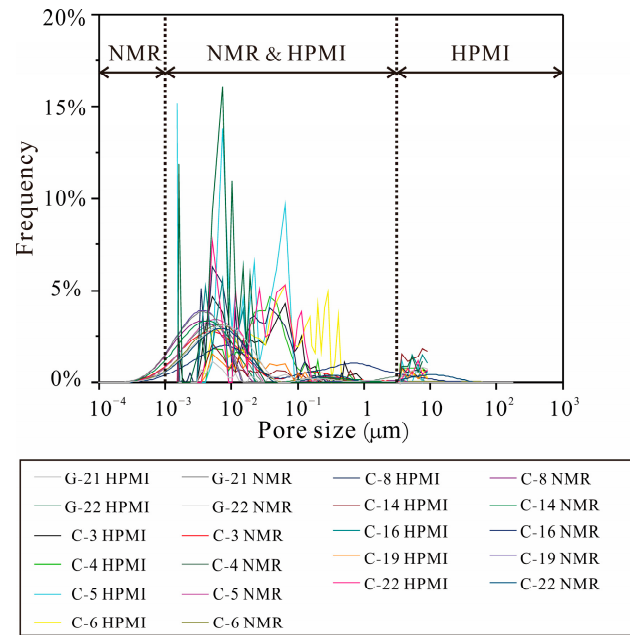


**Figure 8.** Combined measurement of pore size distribution in the Longtan tight sandstones in Well CSDP-2 using HPMI and NMR.

### 5.2. Influence of Pore Structure on Petrophysical Properties

To examine the impact of pore homogeneity on petrophysical properties, linear regressions were conducted between the fractal dimensions  $D_{N-1}$  and  $D_{N-2}$  from HPMI,  $D_{N-2}$  from NMR, and the petrophysical properties. The relationships between movable fluid saturation, median radius, and various fractal dimensions were explored to understand the influence of structural parameters on pore structure.

The fractal dimension  $D_{N-1}$  of bound fluid in the Longtan tight sandstones of Well CSDP-2 is below 2.0 (Table 3). Some scholars argue that a fractal dimension distribution outside the range of 2.0 to 3.0 lacks practical significance; for instance, it is logical to assume that if the smoothest part approaches two-dimensional characteristics (described mathematically as  $D \geq 2$ ), the roughest part will exceed this but retain characteristics that are less than three-dimensional ( $D \leq 3$ ) [29,48,49]. However, other opinions suggest that when  $D_{N-1}$  is below 2.0, it mainly reflects the fractal characteristics of bound fluid-occupied pores in a two-dimensional plane. Only fractal dimensions within the range of 2.0 to 3.0 can reflect the three-dimensional fractal characteristics of pores occupied by movable fluids [50]. Therefore, this study focuses on discussing the correlation between  $D_{N-2}$  and petrophysical parameters.

There is no significant correlation between the fractal dimension  $D_{P-1}$  of small pores obtained from HPMI in the studied samples and petrophysical parameters (Figure 9a). In contrast, the fractal dimension  $D_{P-2}$  of large pores obtained from HPMI shows a certain negative correlation with porosity, but no significant correlation with permeability is observed (Figure 9b). A smaller fractal dimension of large pores suggests better homogeneity of reservoir pore structure, implying that large pores with relatively good homogeneity can improve pore connectivity to some extent, but may not significantly enhance reservoir permeability.

The  $D_{N-2}$  of NMR movable fluid in the Longtan tight sandstone samples exhibits a strong negative correlation with reservoir petrophysical properties (Figure 9c), particularly with permeability. Movable fluid mainly occupies pores with radius  $> 0.019 \mu\text{m}$  (Figure 5). The more complex these pore structures are, the stronger the binding effect on fluids inside the pores, leading to decreased fluid mobility within the reservoir [6], thus deteriorating reservoir petrophysical properties, particularly permeability.

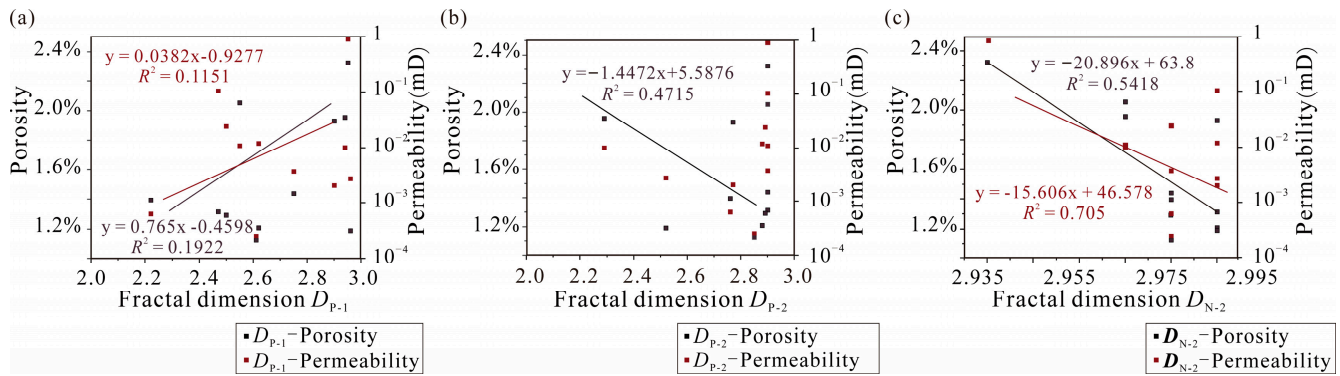


**Figure 9.** Relationship between fractal dimensions and pore permeability of the Longtan tight sandstones of Well CSDP-2. (a) Correlation between fractal dimensions of small pores obtained from HPMI and pore permeability; (b) correlation between fractal dimensions of large pores obtained from HPMI and pore permeability; (c) correlation between fractal dimensions of movable fluid obtained from NMR and pore permeability.

### 5.3. Reservoir Classification Evaluation

The main task of reservoir classification is to evaluate the storage space characteristics and permeability of the reservoir [51]. It requires considering all factors that influence reservoir quality and selecting parameters that can represent the differences in petrophysical properties and pore structure characteristics of various samples, thereby establishing rational and accurate reservoir classification evaluation criteria. In the Longtan Formation tight sandstone samples from Well CSDP-2, there is no significant difference in porosity, while permeability exhibits exponential differences (Table 1). There is a relatively strong positive correlation between the median radius and the  $D_{P-1}$  of small pores obtained from HPMI (Figure 10a), indicating that samples with larger median radius have a higher proportion of small pores in the total pore volume. There is a good negative correlation between NMR movable fluid saturation and the  $D_{N-2}$  of movable fluid (Figure 10b), showing that as the heterogeneity of pores occupied by movable fluids increases, the reservoir storage and permeability becomes weaker. This can also serve as an important parameter for evaluating the relative quality of reservoirs. In addition to these observations, it is crucial to acknowledge the significance of characterizing fluid flow in unconventional reservoirs, which is imperative for optimizing production strategies and enhancing recovery rates in such challenging reservoirs [52–56].

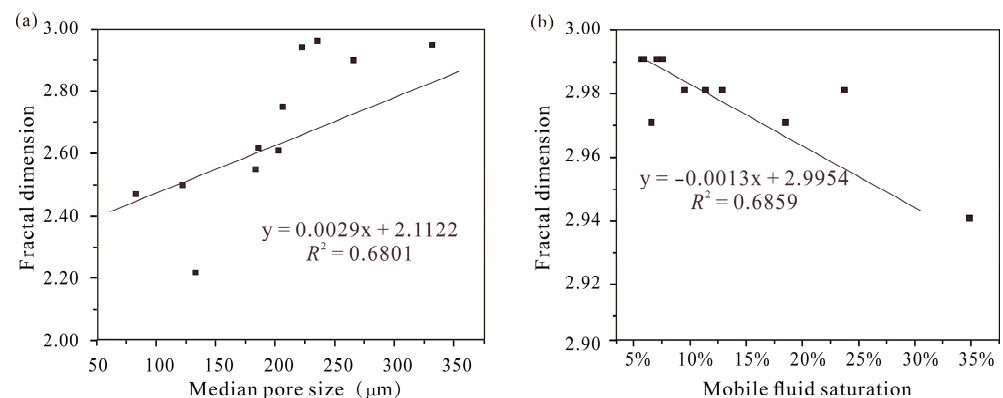


**Figure 10.** Relationship between fractal dimensions and pore structure parameters of the Longtan tight sandstones of Well CSDP-2. (a) Correlation between median radius and fractal dimensions of small pores obtained from HPMI; (b) correlation between movable fluid saturation and fractal dimensions of movable fluid obtained from NMR.

Based on these factors, the studied tight sandstone reservoir in Well CSDP-2 can be divided into three categories (Table 4): Classes I, II, and III. Class I reservoir sandstones (sample C-16) have a relatively high permeability, a movable fluid saturation of 34.82%, a median radius of 331.76  $\mu\text{m}$ , good overall petrophysical properties, and a strong reservoir-seepage capacity. Class II reservoir sandstones (samples G-21, G-22, C-3, C-5, C-6, C-14, C-19, and C-22) have a medium level of permeability, with an average permeability of  $>0.001$  mD, an average movable fluid saturation of 9.91%, a mean median radius of 187.88  $\mu\text{m}$ , moderate overall petrophysical properties, and weaker reservoir-seepage capacity. Conversely, Class III reservoir sandstones (samples C-4 and C-8) exhibit relatively low permeability, with an average permeability of  $<0.001$  mD, an average movable fluid saturation of 6.46%, a mean median radius of 167.53  $\mu\text{m}$ , poor overall petrophysical properties, and almost no reservoir-seepage capacity. Future research on the Longtan tight sandstones should explore the correlation between these reservoir categories and log responses. Such investigation would facilitate the differentiation and mapping of each reservoir sandstone category across multi-well exploration sites, providing a means to predict sweet spots in similar tight sandstone formations. Additionally, addressing the challenges in drilling, completion, and production from unconventional hydrocarbon reservoirs is essential for maximizing the economic potential of such resources and ensuring sustainable energy production in the long term.

**Table 4.** Classification of tight sandstone reservoirs in the Longtan Formation of Well CSDP-2 in the South Yellow Sea Basin.

Sample Type	Permeability/mD	Median Radius / $\mu\text{m}$	Movable Fluid Saturation /%
Class I	0.92	331.76	34.82
Class II	$>0.001$	(265.56, 82.68)/187.88 <sup>1</sup>	(23.71, 5.64)/9.91 <sup>1</sup>
Class III	$<0.001$	(202.47, 132.79)/167.53 <sup>1</sup>	(12.83, 9.50)/6.46 <sup>1</sup>

<sup>1</sup> Note: (maximum value, minimum value)/mean.

## 6. Conclusions

In the Laoshan Uplift of the South Yellow Sea Basin, the Longtan Formation of Well CSDP-2 displays typical characteristics of tight sandstone reservoirs and is predominantly composed of quartz and feldspar. The prevalent pore types include intra-granular dissolution pores, residual inter-granular pores, and minor micro-fractures. High-pressure mercury intrusion (HPMI) analysis revealed mercury saturation ranging from 73.60% to 99.74%, with threshold pressures ranging from 0.003 to 0.079 MPa and median pore radii spanning 82.68 to 331.76  $\mu\text{m}$ . Additionally, NMR testing indicated that movable fluid predominantly occupies pores  $> 0.019$   $\mu\text{m}$ , with saturation varying between 5.65% and 34.83%.

The HPMI-derived pore structure exhibits multiple fractal characteristics, displaying high overall fractal dimensions and pronounced heterogeneity, leading to a discrete pore distribution. While homogeneity in large pores improves connectivity to some extent, it has little impact on reservoir permeability. The fractal dimension  $D_{N-2}$  of movable fluid pore space obtained from NMR ranges from 2.94 to 2.99, indicating significant heterogeneity in fluid-occupied pores. Increased heterogeneity in such pores hinders fluid flow and storage, deteriorating reservoir properties.

By utilizing permeability differences and parameters such as movable fluid saturation and median radius, the Longtan Formation tight sandstones of Well CSDP-2 were classified into three categories. Of these, Class I reservoir sandstones exhibit favorable oil and gas storage and permeability, representing a relatively high-quality reservoir.

**Author Contributions:** Conceptualization, Y.Y.; methodology, H.Z. (Haoran Zhang), Y.Y. and J.L.; software, H.Z. (Haoran Zhang); validation, H.Z. (Haoran Zhang) and Y.Y.; formal analysis, H.Z. (Haoran Zhang); investigation, H.Z. (Haoran Zhang) and Y.Y.; resources, Y.Y., J.C. and J.L.; data curation, H.Z. (Haoran Zhang), Y.Y. and H.Z. (Hualin Zhao); writing—H.Z. (Haoran Zhang); writing—review and editing, H.Z. (Haoran Zhang), Y.Y. and H.Z. (Hualin Zhao); visualization, H.Z. (Haoran Zhang), Y.Y. and H.Z. (Hualin Zhao); supervision, Y.Y., J.C. and J.L.; project administration, J.C. and J.L.; funding acquisition, Y.Y., J.C. and J.L. All authors have read and agreed to the published version of the manuscript.

**Funding:** This research was jointly supported by the National Natural Science Foundation of China (42206234, 42076220), the Project of Laoshan Laboratory (LSKJ202203404, LSKJ202203401), the Project of China Geology Survey (DD20230401, DD20230317, DD20221723, DD20190818), and the Ocean Negative Carbon Emissions Program.

**Institutional Review Board Statement:** Not applicable.

**Informed Consent Statement:** Not applicable.

**Data Availability Statement:** All the data and materials used in this paper are available from the corresponding authors upon request.

**Acknowledgments:** We are grateful to Penghui Zhang for his valuable suggestions on the revision and improvement of this manuscript. We also thank Baxiu Wang for helping with SEM observations.

**Conflicts of Interest:** The authors declare no conflicts of interest.

## References

- Pollastro, R.M. Total petroleum system assessment of undiscovered resources in the giant Barnett Shale continuous (unconventional) gas accumulation, gas accumulation, Fort Worth Basin, Texas. *AAPG Bull.* **2007**, *91*, 551–578. [[CrossRef](#)]
- Zou, C.; Zhu, R.; Wu, S.; Yang, Z.; Tao, S.; Yuan, X.; Hou, L.; Yang, H.; Xu, C.; Li, D.; et al. Types, characteristics, genesis and prospects of conventional and unconventional hydrocarbon accumulations: Taking tight oil and tight gas in China as an instance. *Acta Petrol. Sin.* **2012**, *33*, 173–187.
- Jia, C.; Zou, C.; Li, J.; Li, D.; Zheng, M. Assessment criteria, main types, basic features and resource prospects of the tight oil in China. *Acta Petrol. Sin.* **2012**, *33*, 343–350.
- Li, G.; Zhu, R. Progress, challenges and key issues of unconventional oil and gas development of CNPC. *China Pet. Explor.* **2020**, *25*, 1.
- Zhang, P.; Lee, Y.I.; Zhang, J. A review of high-resolution X-ray computed tomography applied to petroleum geology and a case study. *Micron* **2019**, *124*, 102702. [[CrossRef](#)] [[PubMed](#)]
- Yang, Z.; Zou, C. Orderly “symbiotic enrichment” of conventional & unconventional oil and gas—discussion on theory and technology of conventional & unconventional petroleum geology. *Acta Geol. Sin.* **2022**, *96*, 1635–1653.
- Yao, J.; Liu, X.; Zhao, H.; Li, X. Characteristics of He 8th member tight sandstone gas reservoir and solution based on geology-engineering integration in Ordos Basin. *China Pet. Explor.* **2019**, *24*, 186–195.
- Wang, J.; Zhang, C.; Li, J.; Li, Y.; Li, X.; Liu, P.; Lu, J. Tight sandstone gas reservoirs in the Sulige Gas Field: Development understandings and stable-production proposals. *Nat. Gas Ind.* **2021**, *41*, 100–110.
- Liu, N.; He, K.; Ye, C. Application of geology-engineering integration in the development of tight gas reservoir in Sulige Gasfield. *China Pet. Explor.* **2017**, *22*, 53–60.
- Shi, X.; You, L.; Ge, Y.; Hu, Y.; Ma, L.; Wang, Y.; Guo, S. Water production mechanism in tight sandstone gas reservoirs after fracturing in Linxing Gas Field. *Xinjiang Pet. Geol.* **2024**, *45*, 81–87.
- Zhao, X.; Li, H.; Fu, L.; Cui, Y.; Han, G.; Lou, D.; Pu, X.; Liu, G.; Jiang, W.; Dong, X.; et al. Characteristics, main controlling factors and development mode of Paleozoic coal-formed condensate gas reservoirs in Huanghua depression, Bohai Bay Basin. *Acta Petrol. Sin.* **2021**, *42*, 1592–1604.
- Li, J.; Pu, R.; Wu, Y.; Tian, Y. Sedimentary characteristics and favorable reservoir prediction of Longtan Formation in Huangqiao area, Jiangsu Province. *Pet. Geol. Exp.* **2012**, *34*, 395–399.
- Tobin, R.C.; McClain, T.; Lieber, R.B.; Ozkan, A.; Banfield, L.A.; Marchand, A.M.E.; McRae, L.E. Reservoir quality modeling of tight-gas sands in Wamsutter field: Integration of diagenesis, petroleum systems, and production data. *AAPG Bull.* **2020**, *94*, 1229–1266. [[CrossRef](#)]
- Zhang, P.; Lee, Y.I.; Zhang, J. Diagenesis of tight-gas sandstones from the Lower Cretaceous Dengloulou Formation, Songliao Basin, NE China: Implications for reservoir quality. *J. Petrol. Geol.* **2015**, *38*, 99–114. [[CrossRef](#)]
- Zhang, P.; Lee, Y.I.; Zhang, J. Diagenetic controls on the reservoir quality of tight oil-bearing sandstones in the Upper Triassic Yanchang Formation, Ordos Basin, North-Central China. *J. Petrol. Geol.* **2020**, *43*, 225–244. [[CrossRef](#)]
- Khormali, A.; Ahmadi, S. Prediction of barium sulfate precipitation in dynamic tube blocking tests and its inhibition for waterflooding application using response surface methodology. *J. Petrol. Explor. Prod. Technol.* **2023**, *13*, 2267–2281. [[CrossRef](#)]

17. Fu, Y.; Yan, B.; Liang, J.; Chen, J.; Lei, B.; Wang, M.; Tan, M.; Yang, C.; Yuan, Y.; Zhang, P. Influence of basement high and detachment on the kinematics of a fold-and-thrust belt in the central South Yellow Sea Basin, China: Insights from analog modeling. *Mar. Pet. Geol.* **2024**, *160*, 17. [[CrossRef](#)]
18. Zhang, X.; Guo, X.; Wu, Z.; Xiao, G.; Zhang, X.; Zhu, X. Preliminary results and geological significance of Well CSDP-2 in the Central Uplift of South Yellow Sea Basin. *Chin. J. Geophys.* **2019**, *62*, 197–218. [[CrossRef](#)]
19. Chen, J.; Lei, B.; Liang, J.; Zhang, Y.; Wu, S.; Shi, J.; Wang, J.; Yuan, Y.; Zhang, Y.; Li, G.; et al. New progress of petroleum resources survey in South Yellow Sea basin. *Mar. Geol. Quat. Geol.* **2018**, *38*, 1–23.
20. Lei, B.; Chen, J.; Liang, J.; Zhang, Y.; Li, G. Tectonic deformation and evolution of the South Yellow Sea basin since Indosinian movement. *Mar. Geol. Quat. Geol.* **2018**, *38*, 45–54.
21. Cai, L.; Wang, J.; Guo, X.; Xiao, G.; Zhu, X.; Pang, Y. Characteristics of sedimentary facies and source rocks of Mesozoic-Paleozoic in Central Uplift of South Yellow Sea: A case study of CSDP-2 coring well. *J. Jilin Univ.* **2017**, *47*, 1030–1046.
22. Yuan, Y.; Chen, J.; Zhang, Y.; Zhang, Y.; Liang, J.; Zhang, P. Sedimentary system characteristics and depositional filling model of Upper Permian–Lower Triassic in South Yellow Sea Basin. *J. Cent. South Univ.* **2018**, *25*, 2910–2928. [[CrossRef](#)]
23. Cai, L.; Xiao, G.; Guo, X.; Wang, J.; Wu, Z.; Li, B. Evaluation of Upper Paleozoic and Mesozoic source rocks in Well CSDP-2 and marine oil & gas exploration prospect in the South Yellow Sea Basin. *Acta Petrol. Sin.* **2018**, *39*, 660–673.
24. Xiao, G.; Cai, L.; Guo, X.; Zhang, X.; Wu, Z. Mesozoic-Paleozoic petroleum geological characteristics revealed by CSDP-2 Well in the South Yellow Sea of the “Continental Shelf Drilling Program”. *Mar. Geol. Lett.* **2019**, *35*, 73–76.
25. Yuan, Y.; Chen, J.; Liang, J.; Zhang, Y.; Xue, L.; Wu, S.; Lan, T.; Wu, P. Characteristics and hydrocarbon prospects of the Permian sandstone reservoirs of the Laoshan Uplift, South Yellow Sea. *Mar. Geol. Quat. Geol.* **2021**, *41*, 181–193.
26. Yang, Y.; Yi, C.; Li, G. Sequence stratigraphic identification and geologic age inference of seismic profiles in Central Uplift, South Yellow Sea. *Mar. Orig. Pet. Geol.* **2015**, *20*, 49–56.
27. Zhang, P.; Huang, H.-H.M.; Hong, Y.; Tian, S.Y.; Liu, J.; Lee, Y.I.; Chen, J.; Liang, J.; Wang, H.; Yasuhara, M. Southward migration of Arctic Ocean species during the Last Glacial Period. *Geophys. Res. Lett.* **2022**, *49*, 10. [[CrossRef](#)]
28. Chen, J.; Gong, J.; Li, G.; Li, H.; Yuan, Y.; Zhang, Y. Great resources potential of the marine Mesozoic-Paleozoic in the South Yellow Sea Basin. *Mar. Geol. Front.* **2016**, *32*, 1–7.
29. Pfeifer, P.; Avnir, D. Chemistry in noninteger dimensions between two and three. I. Fractal theory of heterogeneous surfaces. *J. Chem. Phys.* **1983**, *79*, 3558–3565. [[CrossRef](#)]
30. Li, K. Analytical derivation of Brooks-Corey type capillary pressure models using fractal geometry and evaluation of rock heterogeneity. *J. Pet. Sci. Eng.* **2010**, *73*, 20–26. [[CrossRef](#)]
31. Liu, X.; Xiong, J.; Liang, L. Investigation of pore structure and fractal characteristics of organic-rich Yanchang formation shale in central China by nitrogen adsorption/desorption analysis. *J. Nat. Gas Sci. Eng.* **2015**, *22*, 62–72. [[CrossRef](#)]
32. Li, K.; Horne, R.N. Fractal modeling of capillary pressure curves for The Geysers rocks. *Geothermics* **2006**, *35*, 198–207. [[CrossRef](#)]
33. Jiang, Y.; Xu, G.; Bi, H.; Shi, Y.; Gao, Y.; Han, X.; Zeng, X. A new method to determine surface relaxivity of tight sandstone cores based on LF-NMR and high-speed centrifugation measurements. *J. Pet. Sci. Eng.* **2021**, *196*, 108096. [[CrossRef](#)]
34. Nabawy, B.S.; Géraud, Y.; Rochette, P.; Bur, N. Pore-throat characterization in highly porous and permeable sandstones. *AAPG Bull.* **2009**, *93*, 719–739. [[CrossRef](#)]
35. Wu, S.; Zhu, R.; Li, X.; Jin, X.; Yang, Z.; Mao, Z. Evaluation and application of porous structure characterization technologies in unconventional tight reservoirs. *Earth Sci. Front.* **2018**, *25*, 191–203.
36. Yang, S.; Wei, J. *Fundamentals of Petrophysics*; Petroleum Industry Press: Beijing, China, 2004.
37. Shi, J.; Qu, X.; Lei, Q.; Fu, B.; He, Y.; Zhao, G.; Cheng, L. Distribution characteristics and controlling factors of movable fluid in tight oil reservoir: A case study of Chang 7 reservoir in Ordos Basin. *Nat. Gas Geosci.* **2016**, *27*, 827.
38. Wang, W.; Niu, X.; Liang, X.; Dan, W. Characteristic of Movable Fluid for Tight Sandstone Reservoir in Ordos Basin: A Case of Chang 7 Oil Reservoir of Yanchang Formation in Jiyuan Area. *Geol. Sci. Technol. Inf.* **2017**, *36*, 183–187.
39. Ren, Y.; Wu, K.; He, K.; Wu, G.; Zhu, Y.; Wu, H.; Yang, Y. Application of NMR Technique to movable fluid of ultra-low permeability and tight reservoir: A case study on the Yanchang Formation in Longdong Area, Ordos Basin. *J. Mineral. Pet.* **2017**, *37*, 103–110.
40. Wang, Z.; Zhang, C.; Xiao, C.; Chen, X.; Song, F. Experimental study of  $T_{2\text{-cutoff}}$  values in low-permeability reservoirs. *Prog. Geophys.* **2004**, *19*, 652–655.
41. Liu, T.; Ma, Z.; Fu, R. Analysis of rock pore structure with NMR spectra. *Prog. Geophys.* **2003**, *18*, 737–742.
42. Zhao, Y.; Chen, S.; Guo, Z. Application of Nuclear magnetic resonance technology to pore structure in tight sandstone. a case from Third Member of Shihezi Formation Upper Paleozoic in Daniudi Gas Field, Ordos Basin. *Geol. Sci. Technol. Inf.* **2006**, *25*, 109–112.
43. Schmitt, M.; Fernandes, C.; Wolf, F.; Neto, J.; Rahner, C.; dos Santos, V. Characterization of Brazilian tight gas sandstones relating permeability and Angstrom-to micron-scale pore structures. *J. Nat. Gas Sci. Eng.* **2015**, *27*, 785–807. [[CrossRef](#)]
44. Xi, K.; Cao, Y.; Haile, B.G.; Zhu, R.; Jahren, J.; Bjørlykke, K.; Zhang, X.; Hellevang, H. How does the pore-throat size control the reservoir quality and oiliness of tight sandstones? The case of the Lower Cretaceous Quantou Formation in the southern Songliao Basin, China. *Mar. Pet. Geol.* **2016**, *76*, 1–15. [[CrossRef](#)]
45. Liu, G.; Wang, L.; Sun, Z.; Wang, J.; Jiang, F. Research progress of pore-throat structure in tight sandstone formation. *Pet. Sci. Bull.* **2022**, *7*, 406–419.

46. Zhang, Z.; Qin, Y.; Zhuang, X.; Li, G.; Wang, X. Poroperm characteristics of high-rank coals from Southern Qinshui Basin by mercury intrusion, SEM-EDS, nuclear magnetic resonance and relative permeability analysis. *J. Nat. Gas Sci. Eng.* **2018**, *51*, 116–128. [[CrossRef](#)]
47. Liu, Z.; Liu, D.; Cai, Y.; Yao, Y.; Pan, Z.; Zhou, Y. Application of nuclear magnetic resonance (NMR) in coalbed methane and shale reservoirs: A review. *Int. J. Coal Geol.* **2020**, *218*, 15. [[CrossRef](#)]
48. Li, Z.; Shen, X.; Qi, Z.; Hu, R. Study on the pore structure and fractal characteristics of marine and continental shale based on mercury porosimetry, N<sub>2</sub> adsorption and NMR methods. *J. Nat. Gas Sci. Eng.* **2018**, *53*, 12–21. [[CrossRef](#)]
49. Zhu, F.; Hu, W.; Cao, J.; Sun, F.; Liu, Y.; Sun, Z. Micro/nanoscale pore structure and fractal characteristics of tight gas sandstone: A case study from the Yuanba area, northeast Sichuan Basin, China. *Mar. Pet. Geol.* **2018**, *98*, 116–132. [[CrossRef](#)]
50. Shao, X.; Pang, X.; Li, H.; Zhang, X. Fractal Analysis of pore network in tight gas sandstones using NMR method: A case study from the Ordos Basin, China. *Energy Fuels* **2017**, *31*, 10358–10368. [[CrossRef](#)]
51. Ramandi, H.; Mostaghimi, P.; Armstrong, R.; Saadatfar, M.; Pinczewski, W. Porosity and permeability characterization of coal: A micro-computed tomography study. *Int. J. Coal Geol.* **2016**, *154*, 57–68. [[CrossRef](#)]
52. Sorensen, J.A.; Kurz, B.A.; Hawthorne, S.B.; Jin, L.; Smith, S.A.; Azenkeng, A. Laboratory characterization and modeling to examine CO<sub>2</sub> storage and enhanced oil recovery in an unconventional tight oil formation. *Energy Procedia* **2017**, *114*, 5460–5478. [[CrossRef](#)]
53. Zhang, Y.; Zhao, Y.; Lei, X.; Yang, M.; Zhang, Y.; Song, Y. Quantitatively study on methane hydrate formation/decomposition process in hydrate-bearing sediments using low-field MRI. *Fuel* **2020**, *262*, 116555. [[CrossRef](#)]
54. Hassanpouryouzband, A.; Joonaki, E.; Farahani, M.V.; Takeya, S.; Ruppel, C.; Yang, J.; English, N.J.; Schicks, J.M.; Edlmann, K.; Mehrabian, H.; et al. Gas hydrates in sustainable chemistry. *Chem. Soc. Rev.* **2020**, *49*, 5225–5309. [[CrossRef](#)] [[PubMed](#)]
55. Farahani, M.V.; Guo, X.; Zhang, L.; Yang, M.; Hassanpouryouzban, A.; Zhao, J.; Song, Y.; Tohidi, B. Effect of thermal formation/dissociation cycles on the kinetics of formation and pore-scale distribution of methane hydrates in porous media: A magnetic resonance imaging study. *Sustain. Energy Fuels* **2021**, *5*, 1567–1583. [[CrossRef](#)]
56. Pearce, J.; Raza, S.; Baublys, K.; Hayes, P.; Firouzi, M.; Rudolph, V. Unconventional CO<sub>2</sub> storage: CO<sub>2</sub> mineral trapping predicted in characterized shales, sandstones, and coal seam interburden. *SPE J.* **2022**, *27*, 3218–3239. [[CrossRef](#)]

**Disclaimer/Publisher’s Note:** The statements, opinions and data contained in all publications are solely those of the individual author(s) and contributor(s) and not of MDPI and/or the editor(s). MDPI and/or the editor(s) disclaim responsibility for any injury to people or property resulting from any ideas, methods, instructions or products referred to in the content.